NANO LETTERS

Letter

pubs.acs.org/NanoLett

Extraordinary Nonlinear Absorption in 3D Bowtie Nanoantennas

Jae Yong Suh,[†] Mark D. Huntington,[‡] Chul Hoon Kim,[†,§] Wei Zhou,[‡] Michael R. Wasielewski,[†,§] and Teri W. Odom*[,†,‡,§]

[†]Department of Chemistry, [‡]Department of Materials Science and Engineering, and [§]Argonne-Northwestern Solar Energy Research (ANSER) Center, Northwestern University, Evanston, Illinois 60208, United States

Supporting Information

ABSTRACT: This paper reports that arrays of three-dimensional (3D), bowtie-shaped Au nanoparticle dimers can exhibit extremely high nonlinear absorption. Near-field interactions across the gap of the 3D bowties at the localized surface plasmon resonance wavelengths resulted in an increase of more than 4 orders of magnitude in local field intensity. The imaginary part of the third-order nonlinear susceptibility (Im $\chi^{(3)}$) for the 3D bowtie arrays embedded in a dielectric material was measured to be 10^{-4} esu, more than 2 orders of magnitude higher than reported for other metal nanoparticle-dielectric composites. Moreover, 3D dimers with increased nanoscale structure (such as folding) exhibited increased optical nonlinearity. These 3D nanoantennas can be used as critical elements for nanoscale nonlinear optical devices.

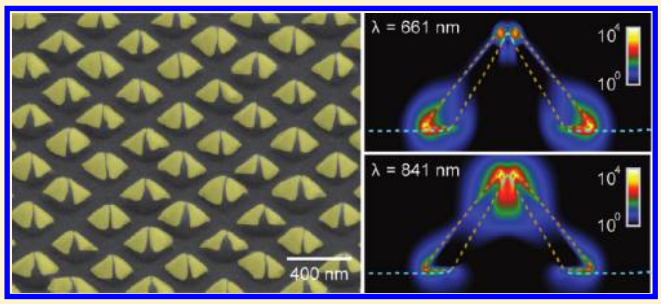

KEYWORDS: *Optical nanoantenna, localized surface plasmons, plasmon hybridization, local field enhancement, nonlinear optical susceptibility*

Dimers of metal nanoparticles (NPs) and individual, anisotropic metal NPs can function as optical nanoantennas.[1−5] The extremely high electric field enhancements within the gap originate from the near-field interactions between the NPs, which produce large field gradients at the localized surface plasmon (LSP) resonance wavelength.[6] Localized fields around metal NPs can also influence their nonlinear optical response;[7−10] however, a range of nonlinear absorption values have been reported[11] because of nonuniform NP filling within the dielectric host and limited field enhancements from single metal NPs. Here we report how an ordered array of three-dimensional (3D) Au bowties can exhibit an extraordinary nonlinear response because of additional localized electric field enhancements from the 3D structure of the NP dimer. Optical transmission measurements revealed that the bowties supported both bonding and antibonding LSP resonances, and finite-difference time-domain (FDTD) calculations showed very high field intensities within the bowtie gap for the bonding LSP mode. The nonlinear behavior of the 3D Au bowties was characterized through an open-aperture *z*-scan measurement, and the extracted imaginary part of the third-order optical susceptibility (Im $\chi^{(3)}$) was found to be at least 2 orders of magnitude higher than previous reports for colloidal Au-dielectric composites.[12,13]

Figure 1 depicts the fabrication process for two different types of 3D Au bowtie arrays. First, a template consisting of a Cr square hole array over an anisotropically etched Si (100) substrate was prepared following a method similar to ref 14. The main difference was that the cross-section of the photoresist (Shipley 1805) posts were square as a result of two sequential UV exposures (at 90°) through a poly(dimethylsiloxane) phase-shifting mask of recessed, 1D lines spaced by 400 nm.[15] After e-beam deposition of a thin layer of Cr (10 nm) followed by lift-off, 120 nm holes remained in the Cr film. This substrate was then subjected to an anisotropic KOH etch,[16] which produced pyramidal pits with four intersecting Si(111) faces beneath the Cr holes (Figure 1, top).

Next, the template was mounted at an angle ψ relative to the e-beam deposition direction, and then two sequential depositions of Au were performed at azimuthal angles φ_1 and φ_2. The gap distance (d) in the dimer was controlled by adjusting ψ, while φ determined the direction of the major axis of the dimer. Type A bowties were prepared by carrying out the first deposition of Au (30 nm) at φ_1 = 45° to produce a triangular Au NP whose center overlapped the shared edge of two Si(111) faces. The sample stage was then rotated by 180°, and a second deposition (φ_2 = 225°) of the same thickness completed the 3D bowtie (Type A). Similarly, Type B bowties were created using the first deposition at φ_1 = 0° and subsequent angle φ_2 = 180°, which produced particles on opposite Si(111) faces in the Si pit. To remove the 3D Au bowties from the etched Si template, we used a template stripping technique[17] with the transparent epoxy polyurethane (PU).

Received: October 5, 2011
Revised: November 26, 2011
Published: December 13, 2011

 © 2011 American Chemical Society

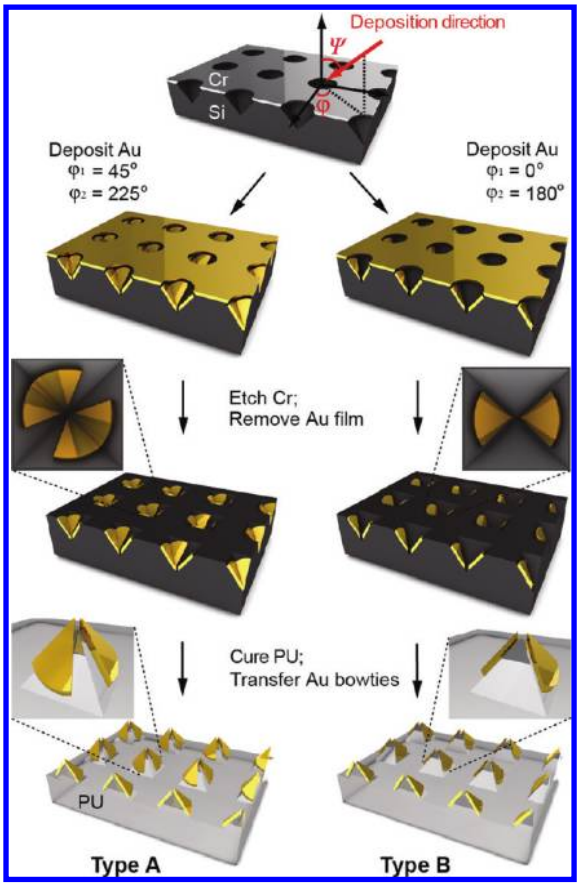

Figure 1. Scheme for fabricating 3D Au bowtie dimers. Two types of bowties (Type A and Type B) can be created starting from a Cr nanohole array on anisotropically etched Si(100) template tilted at angle Ψ. (Left column) Type A bowties were fabricated with a first metal deposition at azimuthal angle φ_1 = 45° and then a second deposition with φ_2 = 225° to complete the dimers. (Right column) Type B bowties were fabricated with a first metal deposition at φ_1 = 0° and a second deposition with φ_2 = 180°. The Cr−Au nanohole film is etched to leave 3D Au bowties in pyramidal Si pits. The dimers can be transferred into an optically transparent material by template stripping with polyurethane.

Because of the parallel nature of the fabrication procedure, cm^2-areas of 3D Au bowties can be fabricated simultaneously. Figure 2 highlights how the two types of bowties have different local curvatures near the gap as well as parallel to the dimer axis because of the different deposition conditions. The small variations in particle shape and gap size are related to variations in the original post size and shape. Figure 2a shows that Type A bowties have a folded edge parallel to the long axis of the dimer because they are produced along the diagonal of the pyramidal pit. Since Type B bowties are formed by NPs on the two opposite Si(111) faces of the pyramidal pit template, the individual NPs are flat with no folding (Figure 2b). Noticeably, the PU surrounding the Au bowtie structures fills the region around the Au dimers, including the gap (Figure 2c).

We measured the linear optical response of arrays of 3D bowties in transmission. Figure 3a displays the normal-incidence spectrum for Type A bowties with an average d = 20 nm when the polarization was parallel to the dimer axis. The two extinction resonances at 660 and 850 nm can be explained in terms of hybridization of localized plasmon resonances,[18−20] where the high-energy dip at λ_- = 660 nm corresponds to an antibonding (−) LSP mode while the smaller low-energy dip at λ_+ = 850 nm is the bonding (+) LSP mode. The bonding mode

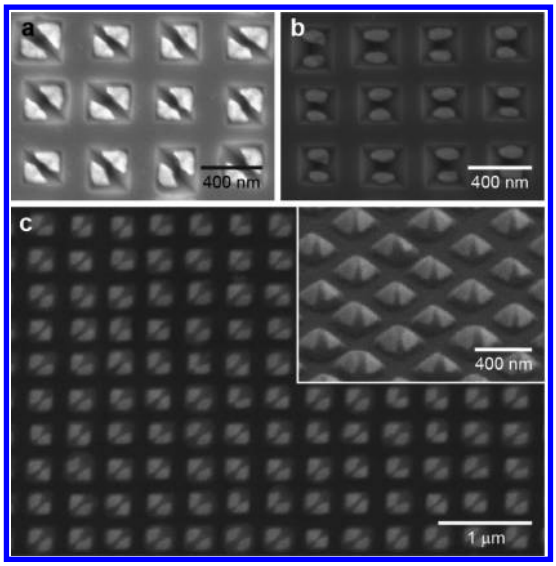

Figure 2. Two types of 3D bowtie nanoantennas can be created from the same template. Scanning electron microscopy (SEM) images of (a) Type A bowties in etched Si template, (b) Type B bowties in etched Si template, and (c) Type A bowties embedded in PU (top-down) and perspective view (inset). Au thickness in each NP was 30 nm, and the lattice spacing for all bowtie arrays = 400 nm.

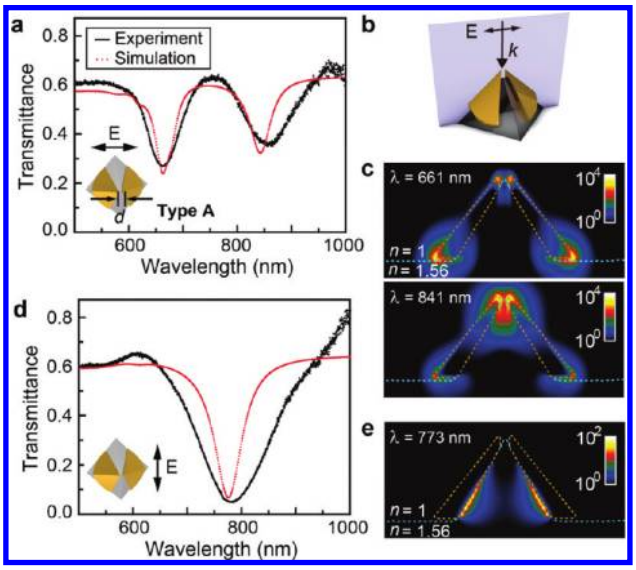

Figure 3. Far-field transmission spectra and near-field calculations of Type A 3D bowties strongly depend on polarization. Type A structures with d = 20 nm support (a) a bonding LSP mode (λ_- = 841 nm) and an antibonding plasmon mode (λ_+ = 661 nm) under normal incidence when the polarization is parallel to the dimer axis. (b) Scheme shows the x−z plane where the field intensities were recorded (bisecting the 3D bowtie). (c) FDTD-calculated $|E|^2/|E_0|^2$ maps at the resonance wavelengths of the plasmon modes show that the high fields within the gap for the bonding mode (λ_+ = 841 nm, $|E|^2_{max}/|E_0|^2 = 2.1 \times 10^4$) are similar to those at the edges for the antibonding mode (λ_- = 661 nm, $|E|^2_{max}/|E_0|^2 = 1.9 \times 10^4$). Intensity is displayed on a logarithmic scale. (d) Normal incidence transmission when the polarization is perpendicular to the dimer axis only shows one dip at the single particle resonance wavelength. (e) Calculated intensity map of the resonance in (d) shows only very low field intensity, where $|E|^2_{max}/|E_0|^2$ is around 10^2.

dx.doi.org/10.1021/nl2034915 | Nano Lett. 2012, 12, 269−274

appears at longer wavelengths because the attractive near-field interactions across the gap lower the resonant frequency.[21] The strength of plasmon hybridization was measured by changing d along the dimer axis, which is parallel to the polarization direction of the incident light (Supporting Information, Figure S1a). The resonance of the low-energy mode blue shifted by 100 nm as the gap distance d increased from ca. 5 to 35 nm. Therefore, the bonding LSP mode became weaker as the gap size increased and approached that of a single particle. Under perpendicular polarization, however, the relatively broad resonance centered at 800 nm did not change significantly (±20 nm) for all gap sizes (Supporting Information, Figure S1b). This result is expected because the effective particle size along the perpendicular polarization direction is similar for all gap sizes.

Electromagnetic field distribution maps calculated by finite-difference time-domain (FDTD) methods (Lumerical Inc., Supporting Information) show in the $x-z$ plane represented in Figure 3b that the strongest fields in the gap are highest at the bonding mode $\lambda_+ = 840$ nm (Figure 3c). Similar intensity fields are localized at the base edges of each NP for the antibonding mode $\lambda_- = 660$ nm. For the bonding mode, the electric field intensity $|E|^2$ near the bowtie tips is enhanced up to 2.1×10^4 compared to the intensity of the incident light $|E_0|^2$. In addition, the normalized field intensity for the bonding mode ($\lambda_+ = 840$ nm) is 1 order of magnitude higher at the midpoint in the gap compared to that of the antibonding mode ($\lambda_- = 660$ nm) at their respective LSP wavelengths (Supporting Information, Figure S2a). When the polarization was perpendicular to the dimer axis (Figure 3d), however, only a single dip was found at $\lambda_p = 780$ nm because the two particles no longer coupled to each other. The electric field distribution map calculated at the single particle wavelength $\lambda_p = 773$ nm does not show enhancements in the gap region (Figure 3e).

In contrast to Type A dimers, Type B bowties with an average $d = 35$ nm did not show two well-defined resonances when the polarization was parallel to the dimer axis (Figure 4a). The only distinctive feature was a low-energy resonance at 810 nm that dominated a very small high-energy resonance. The calculated field distribution map in the $x-z$ plane in Figure 4b at $\lambda_+ = 810$ nm indicates that the resonance has bonding mode LSP character (Figure 4c). FDTD simulations at the wavelength of the small dip ($\lambda_- = 669$ nm) show only very weak field intensities at the flat edges (parallel to PU pyramidal base) of the Au NPs since such structural features cannot concentrate the fields in an antisymmetric charge distribution. This lack of structural folding of the individual NPs within the Type B bowties compared to the Type A bowties therefore produces a weak antibonding LSP, which was not observed in experiment. Similar to the effect in Type A bowties, when the polarization was perpendicular to the Type B dimer axis (Figure 4d), the resonant wavelength was determined only by the effective particle size, and there was no field enhancement in the gap (Figure 4e). The LSP resonances from Type B, however, were noticeably broader than the calculated dip. We attribute this overlap in wavelength position but this difference in resonance line width to a relatively wide range of NP sizes/gaps because Type B structures cannot be fabricated with as much control as Type A ones. For example, during the deposition with $\varphi_1 = 0°$ or $\varphi_2 = 180°$, small amounts of Au can be deposited beyond that on a single Si(111) face, which would result in Au NPs with a majority flat face and minor folds/wings near the edge.

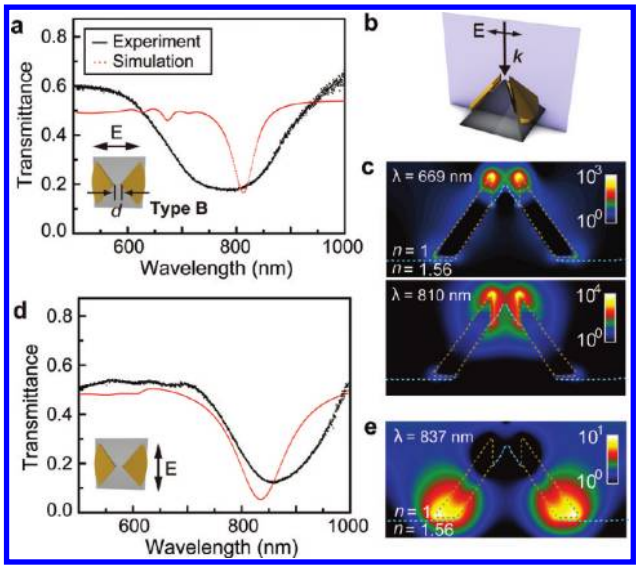

Figure 4. Different 3D geometries of Au bowties can result in very different far-field and near-field properties. Type B structures with d = 35 nm show (a) a strong resonance under normal incidence when the polarization is parallel to the dimer axis and. (b) Scheme shows the $x-z$ plane where the field intensities were recorded (bisecting the 3D bowtie). (c) $|E|^2/|E_0|^2$ map at the calculated resonance wavelength of the bonding plasmon mode ($\lambda_+ = 810$ nm, $|E|^2_{max}/|E_0|^2 = 1.5 \times 10^4$) also shows 4 orders of magnitude enhancement but is 1.4 times less than Type A bowties in Figure 3. Simulations reveal a weak antibonding mode ($\lambda_- = 669$ nm) not observed in experiment with $|E|^2_{max}/|E_0|^2 = 5.52 \times 10^3$. (d) Normal incidence transmission when the polarization is perpendicular to the dimer axis only shows one dip at the single particle resonance wavelength. (e) Calculated intensity map of the resonance in (d) shows very low field intensities, where $|E|^2_{max}/|E_0|^2$ is less than 10.

Angle-resolved zero-order transmission measurements (λ versus θ) converted to energy E versus in-plane wavevector k revealed that the LSP modes are nondispersive for both Type A and Type B 3D bowtie structures (Supporting Information, Figure S3). However, when these resonances crossed the air (−1, 0) or PU (−1, 0) Rayleigh anomaly line,[22] diffractive coupling reduced the extinction intensity at Rayleigh cutoff wavelengths. The suppression of the LSP resonance in a periodic NP array is expected at grazing angles of incidence,[23,24] where the in-plane diffracted waves interact with the NP dimers in the lattice.

The linear response of this metal−dielectric structure, 3D Au bowties surrounded by air on one side and PU on the other, were characterized at the wavelength of the LSP resonance. We combined the linear optical transmittance (T) measurements in Figures 3 and 4 as well as independent reflectance (R) measurements to determine the absorbance $A = 1 - T - R$. This quantity is related to the linear absorption coefficient α by $\alpha = -\log(A)/L$ (cm^{-1}) for the air−Au bowtie array-PU structure, where L is the path length. The linear absorption coefficients α_A and α_B at 780 nm under polarization parallel to the dimer axis were found to be 1.39×10^5 cm^{-1} and 1.84×10^5 cm^{-1} for the Type A and Type B bowties, respectively.

To characterize the nonlinear optical properties of the 3D bowtie nanoantennas, we used the open aperture z-scan technique to determine the imaginary part of $\chi^{(3)}$. Z-scan is a transmittance measurement where the incident irradiance (W/cm^2) of a single, focused laser beam is varied. To induce a third-order nonlinear response, ultrashort laser pulses with

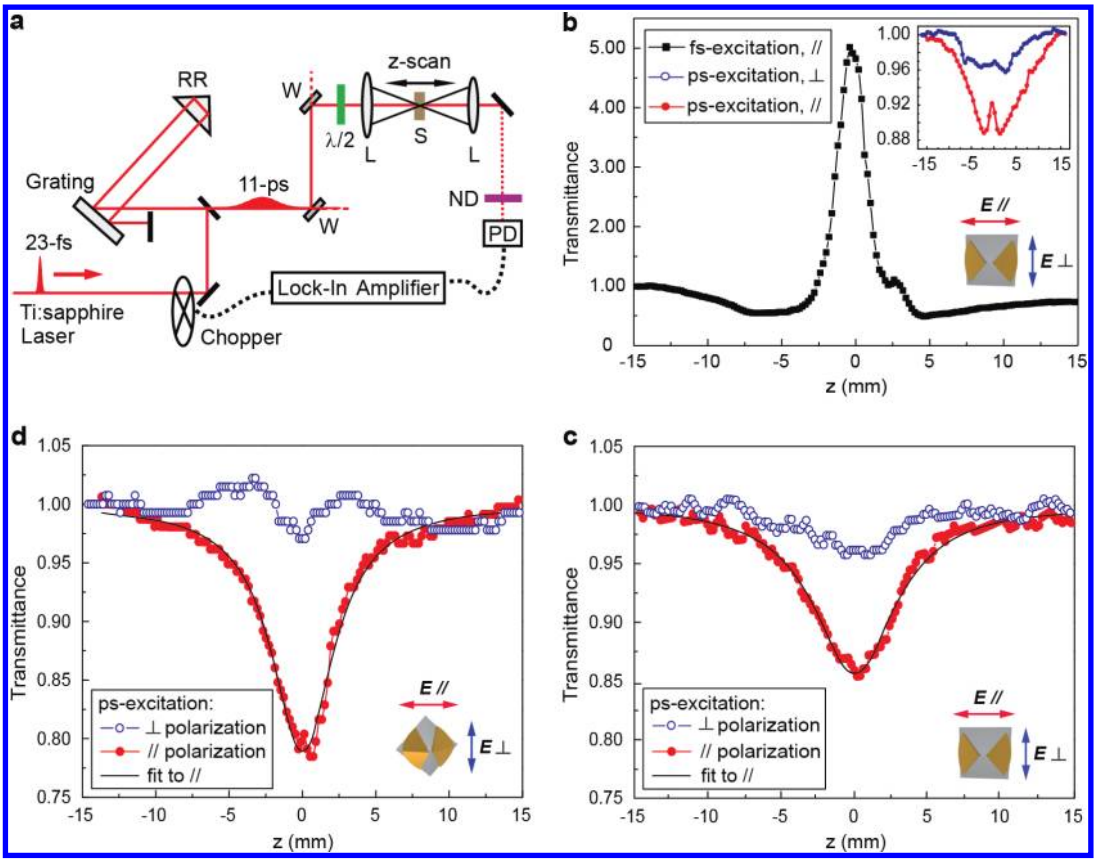

Figure 5. Structural differences of 3D bowties affect their nonlinear absorption properties. (a) Scheme of open aperture z-scan measurement setup. RR, retro-reflector, W, window of 3.4% reflection; $\lambda/2$, half-wave plate; L, lens of 10 cm focal length; S, sample; ND, adjustable neutral density filter; and PD, Si photodiode. Laser wavelength = 780 nm. (b) Normalized z-scan transmission for Type B bowties with 25 fs pulse width (4 nJ) shows a peak at $z = 0$, which indicates a negative nonlinear absorption coefficient β. (b, inset) Transmittance for Type B bowties with 11 ps pulse width (0.8 pJ). Transmittance for (c) Type A bowties and (d) Type B bowties with 11 ps pulse widths (0.5 pJ) for polarizations parallel (//, red solid dots) and perpendicular (⊥, blue empty dots) to the dimer axis. The parallel-polarization curves were fit to the Sheik-Bahae model to calculate the third-order susceptibility.

instantaneously high optical fields are needed. Figure 5a depicts the major components of a z-scan measurement. The fs-light source was a home-built, cavity-dumped Ti:sapphire laser pumped by a frequency doubled Nd:YVO_4 laser (Millennia Vs, Spectra-Physics) (5 W). The center wavelength and spectral width of the cavity-dumped laser output were 780 and 40 nm, respectively. The pulse duration at the sample position without stretching was ~25 fs; femtosecond-pulses were stretched to picoseconds by using a single grating and a Au-coated retro-reflector (RR). The laser beam was focused on the sample with a 100 mm focal length lens, which excited ca. 5×10^3 Au bowties at the focus (beam waist = 27 μm). Two wedged silica windows were used to reduce the laser power, and a broadband $\lambda/2$ waveplate was used to control the polarization of the laser pulse.

The z-scan transmission measurements using 25 fs pulses at 780 nm showed a pronounced peak at $z = 0$ for Type B bowties (Figure 5b), which is a signature of strong saturable absorption.[12] This induced transparency indicates that the ground state has been rapidly depleted under femtosecond-excitation. To extract the nonlinear absorption coefficient β, which is then used to calculate the imaginary part of $\chi^{(3)}$, we used the Sheik-Bahae model[25] to fit the z-scan transmittance $T(z)$

$$T(z) = \sum_{m=0}^{\infty} \frac{\left(\dfrac{-\beta I_0 L_{\mathrm{eff}}}{1 + \dfrac{z^2}{z_0^2}}\right)^m}{(m+1)^{3/2}} \tag{1}$$

where I_0 is the peak intensity at the focus, the effective interaction length $L_{\mathrm{eff}} = [1 - \exp(-\alpha L_c)]/\alpha$, L_c is the film thickness of Au−PU composite, and the Rayleigh diffraction length $z_0 = k\omega_0/2$. $T(z)$ was determined experimentally by measuring the normalized transmission as a function of sample distance z from the focal point of laser beam ($z = 0$). Under femtosecond-excitation, the absolute value of the numerator $|\beta I_0 L_{\mathrm{eff}}|$ in eq 1 becomes greater than 1 for a given nonlinear absorption coefficient β; thus, fitting to the Sheik-Bahae model is not valid because the power series diverges. Therefore, we adjusted the incident pulse width to the picosecond-range by stretching the 25 fs pulse to 11 ps so that I_0 could be reduced by three-orders of magnitude. The inset of Figure 5b shows that with picosecond-excitation (0.8 pJ), a small peak was still present at the focus ($z = 0$) within the valley of the large nonlinear optical absorption, which again indicates the onset of saturable absorption. Third-order nonlinear (multiphoton) absorption has a positive sign of β.[4,26] Although this curve can be fit to the Sheik-Bahae model, we reduced the incident

laser power further to eliminate any ambiguity in the fit when saturable absorption and multiphoton absorption simultaneously exist.[26,27]

Figure 5c,d displays the z-scan transmittances using 11 ps laser pulses (0.5 pJ) for Type B and Type A bowties with d = 35 nm, respectively. This gap distance was chosen since the bonding mode plasmon resonances for both 3D dimers was around λ_+ = 780 nm (Figure 4 and Supporting Information Figure S1), which overlapped the excitation laser wavelength. In the z-scan method, the magnitude of the dip at $z = 0$ directly reflects the strength of the nonlinear absorption coefficient. For Type B bowties, with an average d = 35 nm the transmittance at $z = 0$ dropped from 15% under parallel polarization to just 4% under perpendicular polarization (Figure 5c). For Type A bowties, when the polarization was parallel to the dimer axis, the transmission decreased by 22% at $z = 0$ (Figure 5d). As expected, at the same nonlinear excitation conditions very weak nonlinear signals were measured when the polarization was perpendicular to the dimer axis. This result clearly indicates that the local field effect is more pronounced in Type A bowties compared to Type B ones. Thus, the additional local curvature near the gap region of the Type A dimers results in slightly higher field enhancements compared to Type B dimers because of NP folding in the Type A bowties.

Using the measured β from $T(z)$, we extracted the imaginary part of $\chi^{(3)}$ by the following relation

$$\mathrm{Im}\,\chi^{(3)}\,(\mathrm{esu}) = \frac{c^2 n_0^2 \beta}{640\pi^3\omega} \tag{2}$$

where n_0 is the linear refractive index of Au, and ω is the angular frequency of the laser field. In Figure 5c,d, the best fit values of β and Im $\chi^{(3)}$ were found according to eqs 1 and 2 for each bowtie structure. We determined values of Im $\chi^{(3)}$ to be 3.5×10^{-4} esu for Type A bowties and 2.7×10^{-4} esu for Type B structures. These values for Im $\chi^{(3)}$ are at least 2 orders of magnitude higher than the values for Au NPs reported previously, which ranged from 10^{-6} to 10^{-9} esu depending on the NP sizes, Au volume fraction, and host materials.[8,12,13,27−32] We note that not all previous z-scan measurements were performed at the LSP resonance, which is crucial for large local field factors near the metal NPs. Nevertheless, we have at least a 1000-fold increase in Im $\chi^{(3)}$ because of strong near-field coupling between metal NPs in a dimer compared to a single NP[12,13] and a 100-fold increase compared to the largest reported values from coupled NP systems.[27,32]

In conclusion, we have designed a fabrication method that can produce arrays of 3D bowtie antennas with extremely high electric field localizations. The two different types of Au bowties support strong near-field interactions with local field intensity enhancements $>10^4$, which result in extraordinarily high third-order nonlinear susceptibility values (10^{-4} esu). Therefore, these 3D bowties function as nonlinear optical antennae. We anticipate that these coupled metal NP arrays can be integrated with nonlinear host materials of importance for applications in nonlinear optical devices. These 3D bowties can facilitate the demonstration of nanoscale, nonlinear optical devices, such as single-photon level transistors,[33] plasmonic second-harmonic generators,[34] or lasing nanoresonators.[35]

■ ASSOCIATED CONTENT

Supporting Information

Normal incident transmission spectra for different bowtie gap sizes; FDTD calculated cross-sectional field intensity profile for sample Type A dimer; and angle-resolved transmission spectra for Type A and Type B dimers under p-polarized light. This material is available free of charge via the Internet at http://pubs.acs.org.

■ AUTHOR INFORMATION

Corresponding Author

*E-mail: todom@northwestern.edu.

■ ACKNOWLEDGMENTS

This work was supported by the NSF-MRSEC program at the Materials Research Science and Engineering Center at Northwestern University (DMR-0520513) (J.Y.S., W.Z.) and the NIH-Director's Pioneer Award (DP1OD003899) (J.Y.S., T.W.O). M.D.H acknowledges support by the Department of Defense through the National Defense Science and Engineering Graduate Fellowship (NDSEG) Program. We thank J-.C. Yang for early contributions to this project. C.-H.K. was partially supported by the Initiative for Energy and Sustainability at Northwestern (ISEN) and by the NSF. Development of the cavity-dumped Ti:sapphire laser system used for the z-scan measurements (C.-H.K., M.R.W.) was supported as part of the ANSER Center, an Energy Frontier Research Center funded by the U.S. Department of Energy, Office of Science, Office of Basic Energy Sciences, under Award Number DE-SC0001059.

■ REFERENCES

(1) Crozier, K. B.; Sundaramurthy, A.; Kino, G. S.; Quate, C. F. *J. Appl. Phys.* **2003**, *94* (12), 7950−7950.
(2) Hecht, B.; Muhlschlegel, P.; Eisler, H. J.; Martin, O. J. F.; Pohl, D. W. *Science* **2005**, *308* (5728), 1607−1609.
(3) Sundaramurthy, A.; Crozier, K. B.; Kino, G. S.; Fromm, D. P.; Schuck, P. J.; Moerner, W. E. *Phys. Rev. B* **2005**, *72*, 165409.
(4) Schuck, P. J.; Fromm, D. P.; Sundaramurthy, A.; Kino, G. S.; Moerner, W. E. *Phys. Rev. Lett.* **2005**, *94*, 017402.
(5) Brown, L. V.; Sobhani, H.; Lassiter, J. B.; Nordlander, P.; Halas, N. J. *ACS Nano* **2010**, *4* (2), 819−832.
(6) Fischer, H.; Martin, O. J. F. *Opt. Express* **2008**, *16* (12), 9144−9154.
(7) Uchida, K.; Kaneko, S.; Omi, S.; Hata, C.; Tanji, H.; Asahara, Y.; Ikushima, A. J.; Tokizaki, T.; Nakamura, A. *J. Opt. Soc. Am. B* **1994**, *11* (7), 1236−1243.
(8) Ryasnyanskiy, A. I.; Palpant, B.; Debrus, S.; Pal, U.; Stepanov, A. *J. Lumin.* **2007**, *127* (1), 181−185.
(9) Haraguchi, M.; Okamoto, T.; Inoue, T.; Nakagaki, M.; Koizumi, H.; Yamaguchi, K.; Lai, C.; Fukui, M.; Kamano, M.; Fujii, M. *IEEE J. Sel. Top. Quantum Electron.* **2008**, *14* (6), 1540−1551.
(10) Haglund, R. F.; Yang, L.; Magruder, R. H.; Wittig, J. E.; Becker, K.; Zuhr, R. A. *Opt. Lett.* **1993**, *18* (5), 373−375.
(11) Rao, S. V. *J. Mod. Opt.* **2011**, *58* (12), 1024−1029.
(12) Smith, D. D.; Fischer, G.; Boyd, R. W.; Gregory, D. A. *J. Opt. Soc. Am. B* **1997**, *14* (7), 1625−1631.
(13) Piredda, G.; Smith, D. D.; Wendling, B.; Boyd, R. W. *J. Opt. Soc. Am. B* **2008**, *25* (6), 945−950.
(14) Henzie, J.; Lee, M. H.; Odom, T. W. *Nat. Nanotechnol.* **2007**, *2* (9), 549−554.
(15) Zhou, W.; Gao, H. W.; Odom, T. W. *ACS Nano* **2010**, *4* (2), 1241−1247.
(16) Seidel, H.; Csepregi, L.; Heuberger, A.; Baumgartel, H. *J. Electrochem. Soc.* **1990**, *137* (11), 3612−3626.

(17) Zhou, W.; Odom, T. W. *Nat Nanotechnol.* **2011**, *6* (7), 423–427.
(18) Huang, J. S.; Kern, J.; Geisler, P.; Weinmann, P.; Kamp, M.; Forchel, A.; Biagioni, P.; Hecht, B. *Nano Lett.* **2010**, *10* (6), 2105–2110.
(19) Gwo, S.; Yang, S. C.; Kobori, H.; He, C. L.; Lin, M. H.; Chen, H. Y.; Li, C. C.; Kanehara, M.; Teranishi, T. *Nano Lett.* **2010**, *10* (2), 632–637.
(20) Nordlander, P.; Oubre, C.; Prodan, E.; Li, K.; Stockman, M. I. *Nano Lett.* **2004**, *4* (5), 899–903.
(21) Leitner, A.; Rechberger, W.; Hohenau, A.; Krenn, J. R.; Lamprecht, B.; Aussenegg, F. R. *Opt. Commun.* **2003**, *220* (1–3), 137–141.
(22) Gao, H.; McMahon, J. M.; Lee, M. H.; Henzie, J.; Gray, S. K.; Schatz, G. C.; Odom, T. W. *Opt Express* **2009**, *17* (4), 2334–2340.
(23) Kravets, V. G.; Schedin, F.; Grigorenko, A. N. *Phys. Rev. Lett.* **2008**, *101*, 087403.
(24) Vecchi, G.; Giannini, V.; Rivas, J. G. *Phys. Rev. B* **2009**, *80*, 201401R.
(25) Sheik-Bahae, M. S., A. A.; Wei, T.; Hagan, D. J.; van Stryland, E. w. *IEEE J. Quantum Electron.* **1990**, *26*, 760.
(26) Wang, J.; Gu, B.; Wang, H. T.; Ni, X. W. *Opt. Commun.* **2010**, *283* (18), 3525–3528.
(27) Ning, T. Y.; Zhou, Y. L.; Shen, H.; Lu, H.; Sun, Z. H.; Cao, L. Z.; Guan, D. Y.; Zhang, D. X.; Yang, G. Z. *J. Phys. D: Appl. Phys.* **2007**, *40* (21), 6705–6708.
(28) Shen, H.; Cheng, B. L.; Lu, G. W.; Ning, T. Y.; Guan, D. Y.; Zhou, Y. L.; Chen, Z. H. *Nanotechnology* **2006**, *17* (16), 4274–4277.
(29) Ryasnyanskiy, A. I.; Palpant, B.; Debrus, S.; Pal, U.; Stepanov, A. L. *Phys. Solid State* **2009**, *51* (1), 55–60.
(30) Debrus, S.; Lafait, J.; May, M.; Pincon, N.; Prot, D.; Sella, C.; Venturini, J. *J. Appl. Phys.* **2000**, *88* (8), 4469–4475.
(31) Ricard, D.; Roussignol, P.; Flytzanis, C. *Opt. Lett.* **1985**, *10* (10), 511–513.
(32) Zhou, Y. L.; Chen, C.; Ning, T. Y.; Zhang, D. X.; Wang, P.; Ming, H.; Yang, G. Z. *J. Phys. D: Appl. Phys.* **2008**, *41*, 225301.
(33) Chang, D. E.; Sorensen, A. S.; Demler, E. A.; Lukin, M. D. *Nat. Phys.* **2007**, *3* (11), 807–812.
(34) Cai, W.; Vasudev, A. P.; Brongersma, M. L. *Science* **2011**, *333* (6050), 1720–1723.
(35) Zheludev, N. I.; Prosvirnin, S. L.; Papasimakis, N.; Fedotov, V. A. *Nat. Photonics* **2008**, *2* (6), 351–354.